JGR Atmospheres

RESEARCH ARTICLE
10.1029/2018JD029761

Air-Sea Heat and Momentum Fluxes in the Southern Ocean

Vidhi Bharti[1,2], Christopher W. Fairall[3], Byron W. Blomquist[3], Yi Huang[4,5], Alain Protat[6], Peter P. Sullivan[3], Steven T. Siems[1,2], and Michael J. Manton[1]

[1]School of Earth, Atmosphere and Environment, Monash University, Clayton, Victoria, Australia, [2]Australian Research Council Centre of Excellence for Climate System Science, Monash University, Clayton, Victoria, Australia, [3]Physical Sciences Division, National Oceanic and Atmospheric Association, Earth Systems Research Laboratory, Boulder, CO, USA, [4]School of Earth Sciences, University of Melbourne, Parkville, Victoria, Australia, [5]Australian Research Council Centre of Excellence for Climate Extremes, University of Melbourne, Parkville, Victoria, Australia, [6]Australian Bureau of Meteorology, Melbourne, Victoria, Australia

Abstract The Clouds, Aerosols, Precipitation, Radiation, and atmospherIc Composition Over the southeRn oceaN (CAPRICORN) experiment was carried out in March–April 2016 onboard R/V *Investigator* studying momentum (τ), sensible heat (H_s), and latent heat (H_l) fluxes over the Australian sector of the Southern Ocean including over one cyclonic cold-core and one anticyclonic warm-core mesoscale oceanic eddy. The turbulence-based flux measurements obtained with the NOAA PSD flux system employing eddy covariance (EC) and inertial dissipation (ID) methods are compared with those obtained by the Coupled Ocean-Atmosphere Response Experiment (COARE) 3.5 bulk model, and the neutral transfer coefficients are studied. The relative uncertainty between the turbulence-based and COARE 3.5 estimates of τ, H_s, and H_l are 22%, 70%, and 26%, respectively, at 1-hr time scale over the Southern Ocean. Further, the variability in bulk fluxes is investigated with respect to oceanic eddies, precipitation events, atmospheric stability, and extratropical cyclones encountered during the voyage. The main observed variability is an increase in significant wave height or γ_w ($\sim$33%), τ ($\sim$89%), H_s ($\sim$187%), and H_l ($\sim$79%) over the warm eddy as compared to average voyage values. During the passage of six extratropical cyclones, an increase in τ ($\sim$62% average) and a decrease in H_s ($\sim$235%) and H_l ($\sim$79%) is noted in the warm sector, compared to prestorm conditions, but the pattern reverses behind the cold front.

Key Points:
- COARE 3.5 bulk model gives lower mean estimates of wind stress and heat fluxes in the Southern Ocean when compared with observations
- The 10-m-neutral transfer coefficients of momentum and heat fluxes increase with wind speed >5 m/s
- Heat fluxes decrease in the warm sector of extratropical cyclones, but increase behind the cold front

Supporting Information:
- Supporting Information S1

Correspondence to:
V. Bharti,
vidhi.bharti@monash.edu

Citation:
Bharti, V., Fairall, C. W., Blomquist, B. W., Huang, Y., Protat, A., Sullivan, P. P., et al. (2019). Air-sea heat and momentum fluxes in the Southern Ocean. *Journal of Geophysical Research: Atmospheres*, *124*. https://doi.org/10.1029/2018JD029761

Received 4 OCT 2018
Accepted 2 OCT 2019
Accepted article online 22 NOV 2019

Author Contributions:
Conceptualization: Christopher W. Fairall, Byron W. Blomquist, Yi Huang, Alain Protat, Steven T. Siems
Data curation: Christopher W. Fairall, Byron W. Blomquist
Formal analysis: Christopher W. Fairall
Funding acquisition: Christopher W. Fairall, Byron W. Blomquist, Alain Protat, Peter P. Sullivan, Steven T. Siems
Methodology: Christopher W. Fairall, Byron W. Blomquist
Project administration: Christopher W. Fairall, Byron W. Blomquist, Alain Protat, Peter P. Sullivan, Steven T. Siems
Resources: Christopher W. Fairall, Byron W. Blomquist, Yi Huang, Alain Protat, Steven T. Siems, Michael J. Manton
Supervision: Yi Huang, Steven T. Siems, Michael J. Manton
(continued)

1. Introduction

The quantification of the energy budget of the Southern Ocean (SO) remains a challenge in global climate models due to large uncertainties associated with air-sea fluxes (Bourassa et al., 2013; Cerovečki et al., 2011; Dong et al., 2007; Trenberth & Fasullo, 2010). Several past studies have been conducted over the SO to understand the various aspects of momentum (τ), sensible (H_s), and latent (H_l) heat fluxes (Hande et al., 2012; Hausmann et al., 2016; Herman, 2015; Jiang et al., 2012; Messager et al., 2012; Morrow et al., 1992; O'Neill et al., 2003; Schulz et al., 2012; Slonaker & van Woert, 1999; Song & Yu, 2012). Nevertheless, the environmental dependencies of air-sea interaction remain uncertain owing to inadequate reliable sampling and limited research into key intrinsic processes.

The SO is well known for extreme wind-wave conditions where precipitation, sea spray, and cloud cover play crucial roles in determining the air-sea heat and momentum fluxes. The strong winds cause wave-breaking and produce massive amounts of sea spray influencing energy and mass exchange significantly at the interface (Andreas & Monahan, 2000; Richter & Sullivan, 2014). The region is also characterized by intense oceanic eddy activity coupled with the SO storm track due to its unique geographic location. The prominence of mesoscale oceanic eddies in the Antarctic Circumpolar Current due to the polar front substantially contributes to the poleward heat transport and generates the vertical transport of momentum deep into the ocean (Hausmann & Czaja, 2012; Olbers et al., 2012). However, their distinct contributions to the ocean heat budget are yet to be fully resolved despite recent evidence of their influence on marine atmospheric boundary layer turbulence, cloud properties, and precipitation (Bôas et al., 2015; Frenger et al., 2013; Greatbatch et al., 2007). Further, the SO meteorology is dominated by extratropical cyclones where turbulent fluxes can significantly vary within different sectors. Previous studies suggest that surface fluxes are related to

Writing – review & editing: Christopher W. Fairall, Byron W. Blomquist, Yi Huang, Alain Protat, Steven T. Siems, Michael J. Manton

the sea state and affect storm evolution including precipitation (Beare, 2007; Persson et al., 2008). The diurnal variability of sea surface temperature (Kawai & Wada, 2007) and sensible cooling due to rainfall are basic aspects of air-sea interaction yet to be fully understood in the SO.

The global climate community set a goal to resolve individual components of the surface heat budget accurate to within 5 W/m^2 at 1° spatial resolution and 3–6-hr temporal resolution (Curry et al., 2004). However, different surface flux products report large variances and inconsistencies in the magnitude of fluxes over the SO (Liu et al., 2011; Yu et al., 2011). The biases in satellite infrared retrievals of sea surface temperature, large uncertainties of cloud properties, mesoscale eddies, and atmospheric fronts as well as inadequate representation of diurnal fluctuations of sea surface temperature could be potential sources of errors in satellite flux products. Reanalysis models are progressively improving yet their performance must be evaluated over this region.

Acquiring direct flux measurements from ships has several logistical challenges, particularly in high wind regions (>15 ms) but are crucial for the modulation of indirect flux parameterization schemes. The Coupled Ocean-Atmosphere Response Experiment (or COARE) bulk parameterization model for air-sea fluxes was developed initially for implementation in the tropics and midlatitudes (Brunke et al., 2003; Edson et al., 2013; Fairall et al., 2003). Since its publication in 1996 (Fairall et al., 1996), it has become a popular method to estimate turbulent fluxes over the air-sea interface. However, the model has not been extensively validated for polar oceans featuring diverse conditions notably extreme and light wind conditions, rough sea state, extratropical cyclones, mesoscale eddies, and large near-surface ocean temperature gradients.

Considering these issues and the need for new observations, a field campaign was carried out onboard the R/V *Investigator*, named CAPRICORN (Clouds, Aerosols, Precipitation, Radiation, and atmospherIc Composition Over the southeRn oceaN) 2016. The field program was conducted in March–April 2016 to collect high-quality in situ observations of fluxes, clouds, aerosols, precipitation, and ocean properties over the Australian sector of the SO (Mace & Protat, 2018). One of the major objectives was to advance our knowledge of the boundary layer structure and the surface energy budget in this region. One cyclonic cold core eddy (or cold eddy) and one anticyclonic warm core eddy (or warm eddy) were sampled during the voyage.

In the present paper, section 3.1 discusses the comparison between measured and parameterized momentum and heat flux estimates. An evaluation of neutral transfer coefficients with respect to wind speed and the association of momentum flux with wave age is discussed in section 3.2. Further, the paper addresses the basic aspects of flux variability using COARE 3.5 bulk fluxes over oceanic eddies (section 3.3), precipitation (section 3.4), atmospheric stability (section 3.5), and extratropical cyclonic storms (section 3.6) encountered during the voyage. Through the present study, we attempt to understand the physical mechanisms modulating the air-sea interactions over the SO.

2. The CAPRICORN 2016 Experiment

The R/V *Investigator* departed from Hobart (Tasmania) on 14 March 2016, starting from 43°S reaching 53°S, touching the Subantarctic Front and returned Hobart by 15 April 2016. No flux observations were available from 23 to 26 March due to ship maintenance.

This voyage was one of the first efforts to quantify the turbulent fluxes over the Australian sector of the SO including at high wind speeds. Figure 1a depicts the ship track during the voyage along with the marked (dashed ellipses) locations of the cold core and warm core eddies. Figure 1b shows a spatial map of gridded sea level anomalies (GSLA) which was used to identify the nature and location of mesoscale oceanic eddies.

The measurements were taken during multiple transects over the cold eddy for six days from 30 March to 5 April 2016, starting from the western edge of the eddy at 146.01°E, 50.37°S. The size of the cold eddy was approximately 140 × 110 km. The warm eddy was part of a forming meander (roughly 120 km wide) and was sampled for approximately four days starting from 6–10 April 2016. However, only two transects were conducted due to time limitations.

2.1. Instrumentation and Measurement Techniques

The National Oceanic and Atmospheric Administration, Physical Sciences Division (NOAA PSD) air-sea flux system (Table 1) consists of a fast-response turbulence sensor system for wind speed and water vapor

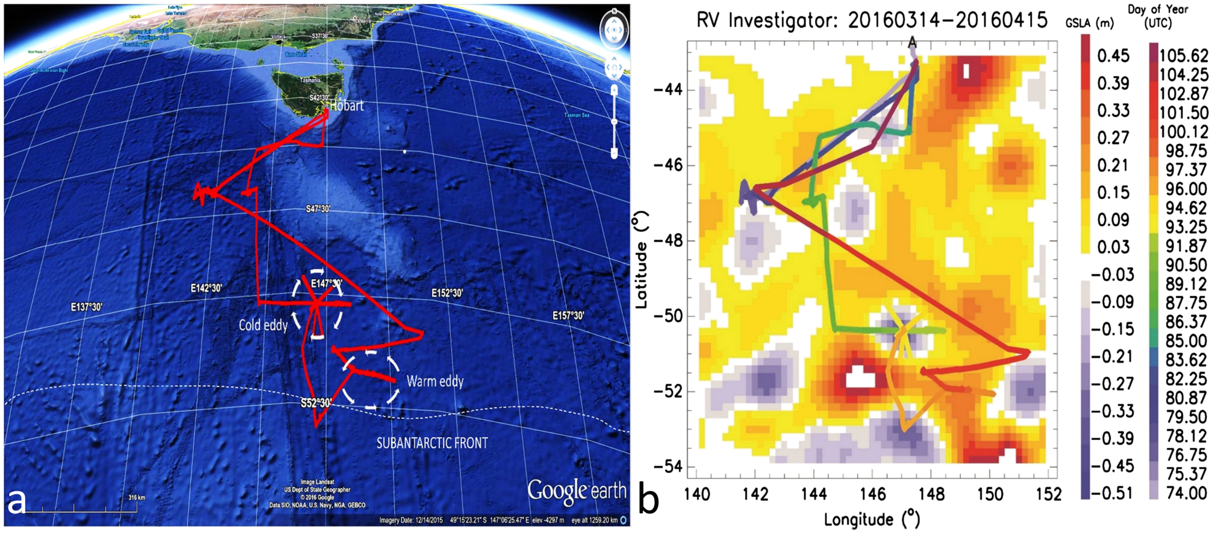

Figure 1. (left) The voyage path of the cruise from 14 March to 15 April 2016. The ship left Hobart and travelled as far south as 53° latitude. (Map developed using Google Earth. earth.google.com/) (right) Map showing the timeline of the voyage in the solar day and gridded sea level anomalies (GSLA) in meters during R/V *Investigator* voyage.

with ship motion corrections; solar and infrared (IR) radiation sensors; bulk pressure, temperature, and humidity sensors; and an optical rain gauge. Most instruments were installed on the bow jackstaff of the ship at a height of 19.5–21m above the water. A sea surface temperature sensor (sea snake) consisting of a floating thermistor (depth ~5 cm) was deployed off the port-side bow outrigger boom. The observations were obtained at a sampling rate of 1 and 10 Hz for slow and fast sensors, respectively. The implementation of the system is discussed in Fairall et al. (1997).

The standard eddy covariance (EC) and inertial dissipation (ID) methods are used for obtaining direct flux measurements (Fairall et al., 1990; Large & Pond, 1981, 1982). The background on the similarity theory and the equations governing the turbulent fluxes are discussed in Fairall et al. (1996), Fairall et al. (2003), and Bradley and Fairall (2006). The ID method is discussed in detail in Appendix B. The description of COARE 3.5 bulk parameterization model can be found in the Supporting information S1.

2.2. Surface and Synoptic Conditions

The voyage summary discusses the surface conditions for each day of the voyage (Trull et al., 2016). The average sunrise to sunset duration lasted from 0600 to 1900 local time, with the voyage enclosing the

Table 1
List of Instruments Onboard R/V Investigator Comprising the NOAA PSD Flux System

Instrument	Parameters	Units	Sensor height (z)	Sampling rate
Ultrasonic 3-axis anemometer (Metek uSonic-3)	Wind speed U_z	m/s	21 m	10 Hz
	Wind direction			
Systron-Donner motion-pak unit	Inertial navigation system			10 Hz
Precision Spectral Pyranometer (Eppley PSP)	Solar downwelling radiative flux	W/m^2	12 m	1 Hz
Precision Infrared Radiometer (Eppley PIR/pyrgeometer)	IR downwelling radiative flux	W/m^2	12 m	1 Hz
Vaisala/HMT335	Air temperature (T_a) Humidity	°C g/kg	19.5 m	1 Hz
Vaisala/PTB220	Pressure	mbar		10 Hz
Floating (YSI 46040) Thermistor, deployed off port side with outrigger (Sea Snake)	Near-skin sea surface temperature (T_s)	°C	−0.05 m	10 Hz
Optical precipitation sensor (ORG-815 DA)	Rain rate	mm/hr	20 m	1 Hz
Li-COR 7500 Open Path CO2/H2O Gas Analyzer	Densities of carbon dioxide and water vapor	kg/m^3	21 m	10 Hz
Riegl laser altimeter	Wave height γ	m	20 m	10 Hz

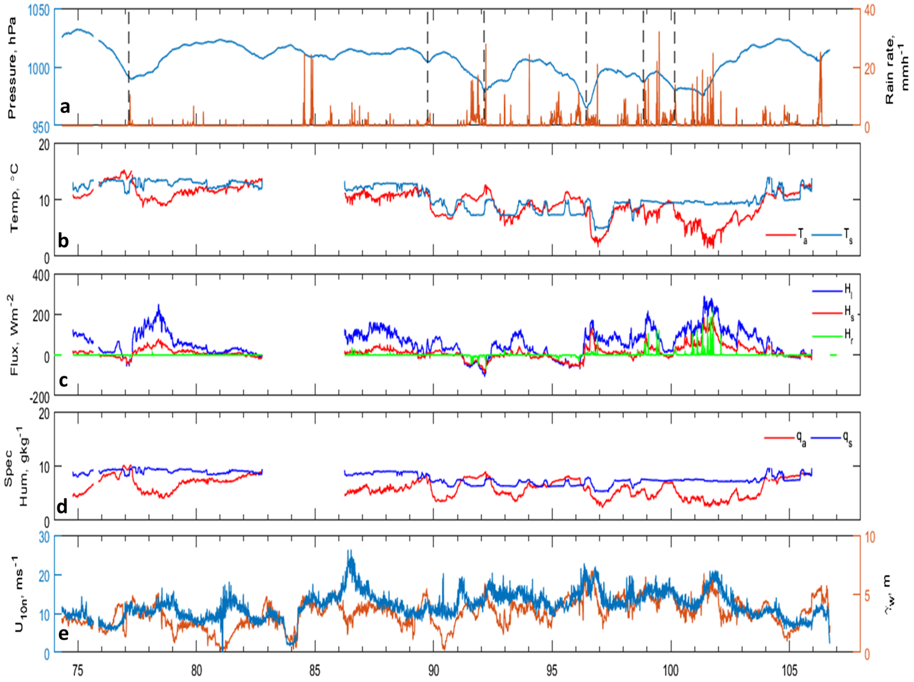

Figure 2. Time series of (a) surface pressure, P, in mbar with passages of cold fronts shown as dashed lines and rain rate in mm/hr. (b) Surface air temperature, T_a, and sea surface temperature, T_s, in °C. (c) Sensible heat flux, H_s; latent heat flux, H_l; and rain heat flux, H_r in W/m^2. (d) Specific humidity, q_a, and sea surface saturation specific humidity, q_s in g/kg. (e) The 10-m neutral wind speed, U_{10n}, in ms and full sea significant wave height, γ, in meters during R/V *Investigator* voyage. The x axis represents the solar day. No flux observations were available from 23 to 26 March due to ship maintenance.

autumnal equinox. Six extratropical cyclones were encountered throughout the voyage. Rainfall was observed ~30% of the voyage duration with the average hourly precipitation rate of 0.56 mm/hr and a maximum rain rate of 19.88 mm/hr. Time series of atmospheric and oceanic measurements are shown in Figure 2. During the voyage, 10-m neutral wind speed, U_{10n}, ranged from 0.40 to ~21 ms, with the average relative wind speed recorded as 10.93 ms.

The sea state can be described using various wave parameters. Earlier research indicated that the Charnock parameter and, in turn, the sea surface roughness should be affected by the fetch and wave steepness, which are functions of wave age and height, respectively (Drennan et al., 2005, and references therein). In the present paper, significant wave height, γ (4 times the RMS surface vertical displacement); wind-sea significant wave height, γ_w; and inverse wave age, (u_*/C_p), are used to define the sea state. The significant wave height, γ, accounts for the open ocean wave field that includes both locally and nonlocally generated waves (i.e., combined wind-sea and swell heights), whereas γ_w is the wave height for local wind-sea waves (i.e., excludes swell). Parameter γ_w is estimated from the 1-D Riegl wave spectra assuming that the wind-sea is in equilibrium with the mean wind. An approximate separation or cutoff frequency (F_w) that partitions the wave spectrum into wind-sea and swell peaks is calculated as $F_w = 0.8 \times g/(2\pi \times U_{10n})$, where g is the acceleration of gravity as described by Gilhousen and Hervey (2002). However, the Doppler correction has not been applied to the laser measurements that might produce a bias to the determination of the wind sea partition at higher wind and ship speeds, as well as our ability to accurately estimate the phase speed of the waves and thereby their wave age. Parameter γ_w is the integral of the wave spectrum from the cutoff frequency up to the high-frequency limit of the data, excluding the low-frequency swell peak. The wave age is defined as, C_p/u_* with $C_p = gT_p/2\pi$ defined as the phase speed of the dominant wave, T_p is spectral peak period and u_* is friction velocity. The nondimensional wave age captures the development of the sea state in response to wind stress over time and has a value of about 30 for a fully developed sea with values below and above it for a younger and decaying sea state, respectively. The inverse wave age (u_*/C_p) is often used because this form compresses the range of old, swell-dominated seas and expands the range of young sea state

Table 2
Details of the Nine Identified Extratropical Cyclones During R/V Investigator Voyage

	From	To
1.	16 March 15 UTC	17 March 14 UTC
2.	29 March 05 UTC	29 March 23 UTC
3.	31 March 05 UTC	01 April 08 UTC
4.	04 April 01 UTC	05 April 05 UTC
5.	06 April 21 UTC	07 April 23 UTC
6.	08 April 12 UTC	09 April 11 UTC

conditions. For a fully developed sea, u_*/C_p is ≈0.03 with larger values indicative of younger sea. u_*/C_p ranges from 0.002 to 0.14 with a mean of 0.029 during the current voyage.

2.3. Identifying Weather Fronts

The traversal of cyclonic storms is associated with sudden changes in wind speed, wind direction, precipitation, and sea state, subsequently impacting surface fluxes. The extratropical cyclones are defined with two criteria: first, hourly Himawari-8 satellite images of cloud top pressure (CTP) and cloud top temperature (CTT) are visually analyzed and the band of clouds having CTP <550 hPa and CTT <−25 °C moving from west to east passing above the ship are associated with the passage of extratropical cyclones. Second, based on the surface observations of pressure (P), temperature (T_a), and wind direction (W), a cyclonic event is identified as when

$$\frac{d^2P}{dt^2}>0.1\ \text{hPa/hr}^2, \frac{dT_a}{dt}<-0.2^\circ\text{C/hr}, \text{and } \frac{dW}{dt}<-5^\circ/\text{hr} \qquad (1)$$

following Wang et al. (2015). Figure 2a identifies cold fronts on the time series of the surface pressure. As outlining the precise boundaries of the warm sector and the cold front is ambiguous, the leading edge of the cloud cover defines the start of the warm sector. Thus, the duration of the cloud band above the ship characterizes the period when the ship is within (or the midst) of the cyclone. The relative minimum of pressure accompanied by precipitation near (mostly just before) the trailing edge of the cloud band defines the location of the cold front. The 12 hr prior to the start of the cloud cover is assumed as precyclonic (or pre) conditions. The 12-hr window after the end of the cloud band defines the postfrontal (or post) conditions. Altogether, nine cyclones were identified during the voyage (Table 2) with two during the cold eddy (31 March and 04 April) and one during the warm eddy (06 April) sampling. The cyclones identified on 23–25 March were discarded due to instrument maintenance. We examined flux variability for strictly prefrontal and postfrontal conditions, noting, however, that prefrontal and postfrontal boundaries of a cyclone are highly variable and difficult to be delineated precisely.

3. Results and Discussion

3.1. Comparison of COARE 3.5 Bulk Fluxes With Turbulent Fluxes

As a result of preliminary quality control, ~48% of the measurements of latent heat flux using EC and ID methods were discarded due to wet conditions and sea salt contamination on the water vapor sensor optics (Licor LI7500). The empirical correction developed for the R/V *Ronald H. Brown* cruise data (Edson et al., 2011; Fairall et al., 2003) is applied to the relative winds to account for flow distortion in the current data set. The bow-mast location and height for the R/V *Investigator* are similar to those of the R/V *Brown*. This correction has been successful on other ships with similar setups (see also Dupuis, 2003, Figure 3).

The 10-min fluxes and associated means were then processed to hourly averages based on an additional set of selection criteria as discussed in Fairall et al. (2003) and Zeng et al. (1998), as follows: (i) relative wind direction with respect to the bow (minimum −60° to maximum 60° with maximum standard deviation 15° over 10 min), (ii) rain rate (maximum 1 mm/hr), (iii) ship speed (maximum standard deviation 0.6 ms and maximum speed 3.5 ms), (iv) ship heading (maximum standard deviation 5°), (v) port-starboard platform velocity from ship roll (maximum standard deviation 0.8 ms), and (vi) flow distortion tilt angle at the top of the bow jack staff (maximum 10°). Figure 3a shows the change in wind stress values with respect to relative wind direction from the bow and change in relative wind direction with respect to the mean airflow tilt angle justifying the criteria (i) and (vi).

The hourly mean turbulent fluxes (average of hourly EC and ID observations) were compared with the hourly COARE 3.5 bulk model outputs (Bariteau et al., 2018). The COARE fluxes are computed with wind speed in the Earth reference frame, which ignores the contribution of surface currents. The ship provided two sources to estimate currents (the 25-m-deep range on the acoustic Doppler current profiler (ADCP)

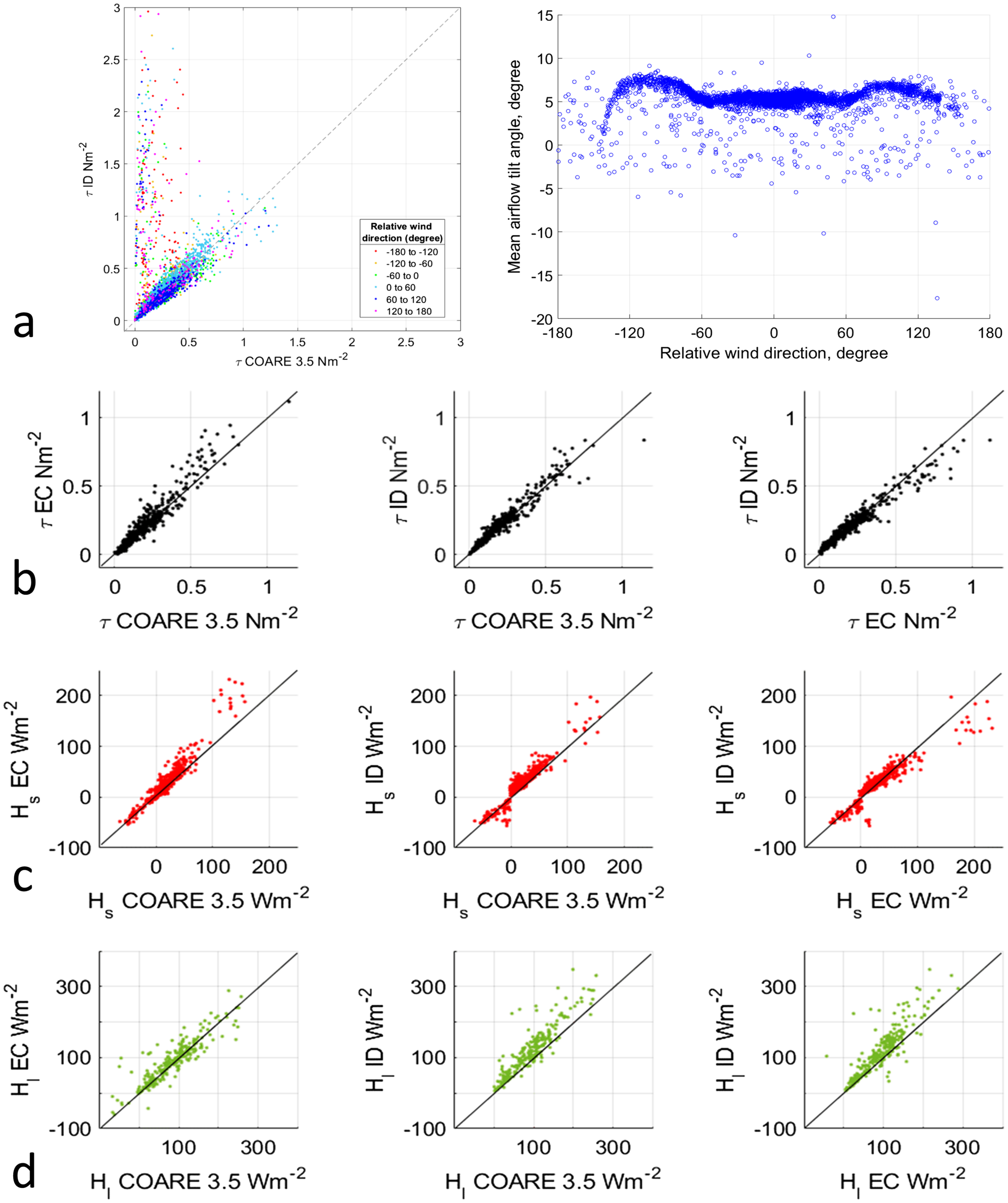

Figure 3. (a, left) Scatterplot between wind stress, τ, obtained by inertial dissipation method (ID) and COARE 3.5 bulk model grouped by relative wind direction (in degree). (right) Scatterplot between relative wind direction (in degree) and mean airflow tilt angle (in degree). Scatterplots for hourly flux values obtained from eddy covariance method (EC), inertial dissipation method (ID), together as the direct method and COARE 3.5 bulk parameterization model for (a) wind stress τ, (b) sensible heat flux H_s, and (c) latent heat flux H_l during R/V *Investigator* voyage. The line represents 1:1 line in all scatterplots.

and a surface drift estimates), but these were poorly correlated, and we decided not to use them. Surface current speeds were measured from the surface drift which gave magnitudes from 0 to 1 ms with an average magnitude of about 0.5 ms. This value represents an error of 8% in τ and 4% in H_s and H_l. H_s and H_l are positive when transporting energy away from the surface (i.e., into the atmosphere). The momentum flux is positive downward (i.e., from the atmosphere to the ocean). Radiation is positive when directed toward the ocean.

Table 3

Error Statistics for Hourly Turbulent Fluxes as Measured by Eddy Covariance (EC) and Inertial Dissipation (ID) Methods and Hourly COARE 3.5 Bulk Fluxes for the Voyage

	Wind stress (445)				Sensible heat flux (445)				Latent heat flux (263)			
	EC	ID	EC + ID	COARE	EC	ID	EC + ID	COARE	EC	ID	EC + ID	COARE
Mean	0.22	0.22	0.22	0.20	24.59	20.60	22.59	15.23	90.01	111.65	100.83	87.42
Average	0.217		0.208		22.59		18.91		100.83		94.13	
RMSE	0.05		0.05		15.77		13.82		38.76		24.55	
Uncertainty = RMSE × 100/Average	22.58		21.99		71.59		70.01		38.44		26.08	
Absolute percent bias	1.28		7.44		16.25		32.59		24.04		13.29	

Note. Sample size for hourly data is given in bracket in the header.

The turbulent and bulk model momentum fluxes correlate strongly ($R^2 = 0.90$) at hourly time scales as shown in Figure 3b. The flux comparisons are summarized in Table 3, which confirms the good agreement in stress. The mean ID value of H_l is higher than both EC and COARE 3.5 values and there is a clear high bias in the Figure 3d scatterplot. The table also shows that the COARE estimates of H_l are in better agreement with EC + ID than the ID estimates are with EC. It also shows that there is a great deal of uncertainty between all three estimates of H_s. The mean value of H_s computed by COARE 3.5 is slightly lower than the EC and ID mean, which is also evident in Figure 3c. The COARE 3.5 estimates of H_l are in good agreement with the EC in the mean and overall as shown in Figure 3d.

The RMS difference between COARE and EC/ID displays a slight increase in H_l during rain events (RMS difference of 30.5 W/m^2) as compared with H_s (RMS difference of 15.5 W/m^2). COARE 3.5 fluxes are lower on average irrespective of wind speed (U_{10n}) and stability conditions (figures not included).

Overall, COARE 3.5 estimates of τ and H_l are in good agreement with our EC values over the SO. COARE 3.5 gives slightly lower estimates of H_s compared with the EC and ID values. However, the significance of the disagreement and EC/ID fluxes with COARE is difficult to evaluate because this is our first experience with this particular sonic anemometer and its characteristics are not well established. Appendix B presents an analysis of the temperature spectra from the Metek sonic anemometer that shows unexplained noise characteristics in weak to moderate temperature forcing. The disagreement between EC and ID fluxes is unusually large and weakens the validity of the comparison.

3.2. Evaluation of Neutral Transfer Coefficients

The neutral transfer coefficient represents the same flux value had the measurements been made at 10-m height in neutral stratification (refer to S1). These are evaluated as functions of U_{10n} and u_*/C_p in the present study. Figure 4 shows the comparison between measured and modeled transfer coefficients with error bars with respect to U_{10n}. The average value of the coefficient is plotted per bin with a width of 1 m/s. However, there are fewer than five data points for <4- and >17-m/s wind speeds; hence, the measured transfer coefficient values are included only for wind speeds 4–17 m/s in the present analysis. We also cannot account for <1-m/s conditions due to the lack of data. Since, there is high uncertainty in H_l values of ID due to unknown reasons, we use H_l values by EC method for the calculation of C_{e10n}.

The agreement is within 10% between measured and modeled C_{d10n} for 4–17-m/s wind speeds. The mean modeled C_{d10n} is $1.3\ (\pm 0.03) \times 10^{-3}$ and both mean modeled C_{e10n} and C_{h10n} are $1.1\ (\pm 0.04) \times 10^{-3}$ for wind speeds 4–17 m/s. The mean measured C_{h10n} (1.4×10^{-3}) is significantly higher than measured C_{e10n} (1.1×10^{-3}), which contradicts the results from COARE and Large and Pond (1982). The measured C_{h10n} initially decreases with wind speed out to 7 m/s and then rises dramatically from a value of 1.1×10^{-3} to 1.9×10^{-3} at 16 m/s. The reason for this behavior and the discrepancy between the heat transfer coefficients is still under investigation. The measured C_{e10n} is at a minimum (0.97×10^{-3}) at 5 m/s but increases with wind speed thereafter consistent with Fairall et al. (2003). The measured C_{e10n} oscillate close to its mean value, that is, from 0.9×10^{-3} at 7 m/s to 1.2×10^{-3} at 15 m/s.

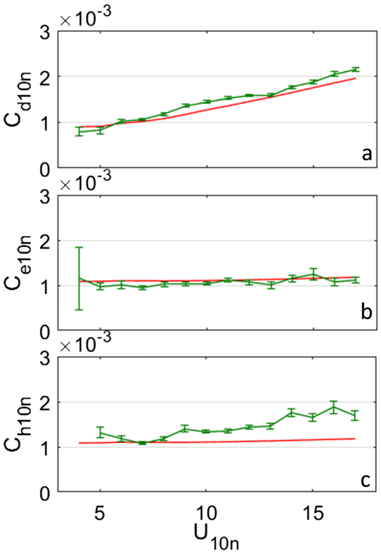

Figure 4. The measured (green) and modeled (red) 10-m neutral transfer coefficient for (a) momentum, C_{d10n} (b) sensible, and C_{h10n} (c) latent heat flux C_{e10n} as a function of 10-m neutral wind speed U_{10n}. Error bars indicate statistical uncertainty of 1 standard deviation divided by the square root of number of observations in the wind speed bin.

The neutral drag coefficient was noted to increase for wind speed >5 m/s and toward low wind speeds in earlier studies (Smith, 1988; Yelland et al., 1998). Fairall et al. (2003) observed a rise in C_{d10n} for winds <1 m/s and at 20 m/s with the minimum value as 1.0×10^{-3} at wind speed 3 m/s. Our calculations show a continuous rise in both bulk and measured C_{d10n} with respect to rising U_{10n}.However, we do not have enough data at wind speeds below 3 m/s to investigate the behavior at low winds.

Surface waves act as the roughness elements that COARE models using the sea surface roughness length that defines the neutral transfer coefficients. The COARE 3.0 and 3.5 algorithms include parameterizations that model the velocity roughness length as a function of specified wave properties such as significant wave height, wavelength of spectral peak, and inverse wave age. However, both versions of COARE have wind-speed-dependent parameterization of the roughness length that match observations well without wave information. Edson et al. (2013) showed that the wave age varies almost linearly with wind speed over the open ocean, which provides an explanation for why wind-speed and wave-age formulations give similar results.

Here, an attempt is made to investigate the wave age and sea-state dependency of the roughness length using the approach described by Donelan et al. (1993). This approach normalizes the roughness length by the significant wave height and plots the normalized height against inverse wave age squared. The roughness length for rough flow, z_0^{rough}, can be calculated as $z_0^{rough} = z_0 - z_0^{smooth} = 10\, e^{-\kappa/C_{d10n}^{0.5}} - 0.11\nu/u_*$ (Edson et al., 2013), where z_0^{smooth} is the roughness of the ocean when it is aerodynamically smooth, z_0 is the total roughness length, κ is the von Kármán's constant, and ν is the kinematic viscosity of air. Previous studies (Dobson et al., 1994; Donelan et al., 1993; Edson et al., 2013; Smith et al., 1992) used this linear approach to explore the association between sea state (specifically wave age) and roughness length:

$$\frac{z_0^{rough}}{\gamma} = D\left(\frac{u_*}{C_p}\right)^2 \tag{2}$$

where D is a numerical constant. Equation (2) is implemented by fitting z_0^{rough}/γ to bin-averaged values of squared u_*/C_p as shown in Figure 5. The measurements used in the present analysis range from 6.9 to 30.4 for C_p, 0.75 to 8.75 for γ, 0.25 to 8.35 for γ_w, and from 0.02 to 1.6 ms for u_*. The measurements used to develop COARE 3.5 gave a value of $D = 0.09$ using the significant wave height to normalize the roughness length (Edson et al., 2013). Using linear regression, the values of D are reported as slightly high with values of 0.128 and 0.117 using γ_w and γ to normalize the roughness length in equation (2), respectively.

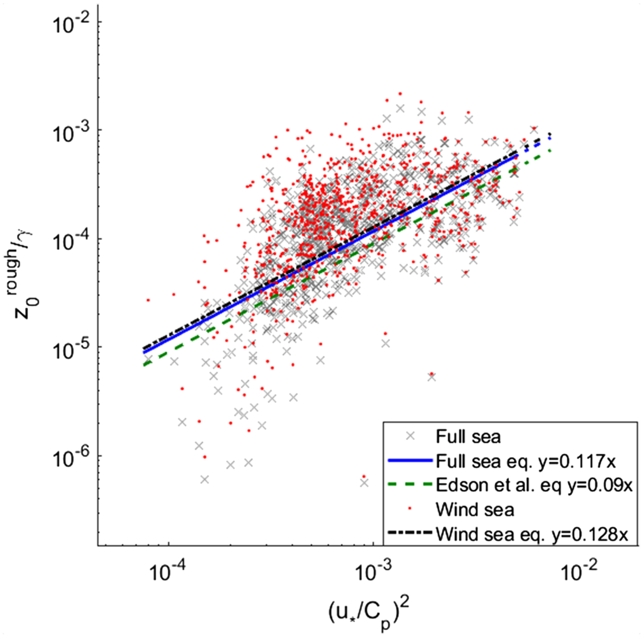

Figure 5. The surface roughness, z_0^{rough}, scaled by significant wave height, γ, as a function of bin-averaged inverse wave age squared on log-log scale. Edson *et al.* represents the relation when $D = 0.09$.

3.3. Flux Variations Over Mesoscale Ocean Eddies

The surface fluxes are convolved with the meteorology (wind speed, air temperature, and humidity) encountered while over the eddies. So, for a small sample, mean fluxes over the sampled eddies may not be representative of the climatological effects of ocean eddies. We have looked at this in two ways. First, we have compared the fluxes in normalized form as a function of the thermal forcing. From the basic bulk flux relationship, we can write

$$\overline{w'X'}/U_{10n} \cong C_{x10n}\Delta X_{10n} \tag{3}$$

Thus, we expect a graph of the covariance divided by U_{10n} to be a linear function of the air-sea difference with a slope given by the transfer

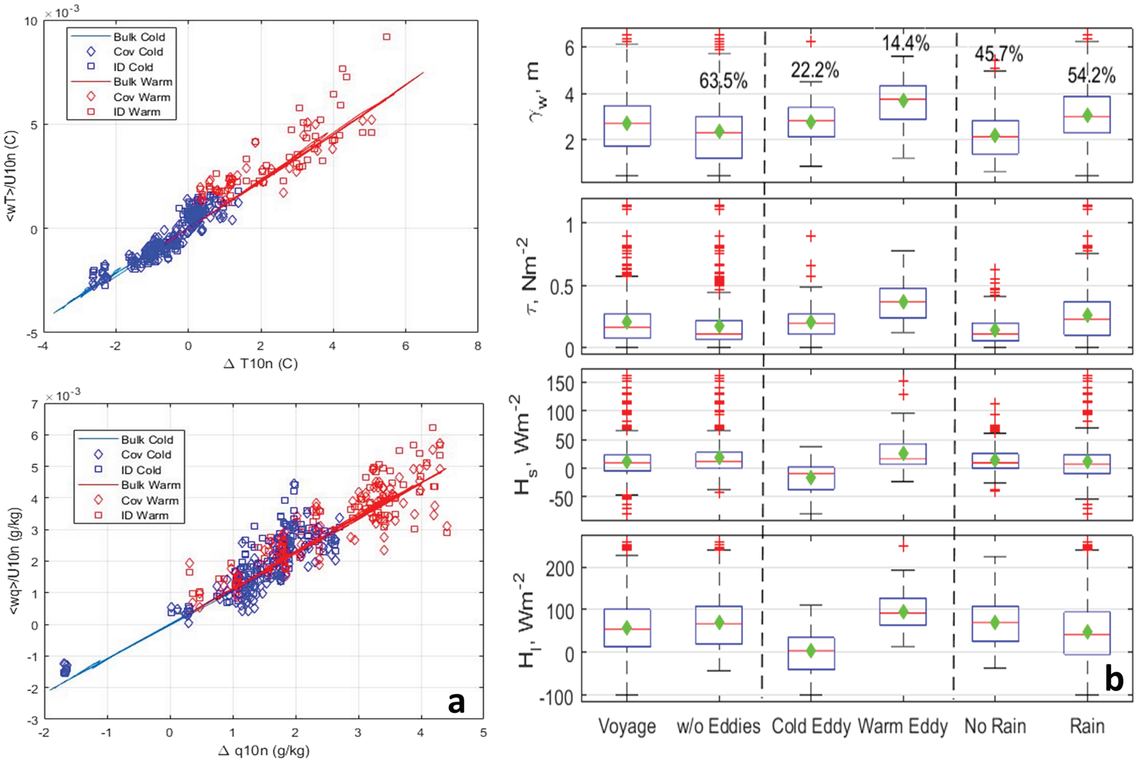

Figure 6. (a) Turbulent flux divided by the neutral 10-m wind speed as a function of the 10-m neutral sea-air difference (top panel—temperature and bottom panel—humidity). The red denotes the warm eddy while the blue denotes the cold eddy. The straight line is the COARE 3.5 bulk value, diamonds the covariance (EC) flux, and squares the ID flux. (b) Wind-sea significant wave height, γ_w (*a*); wind stress, τ (*b*); sensible heat flux, H_S (*c*); and latent heat flux, H_l, distributions (*d*) using COARE 3.5 bulk fluxes during the voyage, over the eddies, and during rainy conditions. A diamond indicates mean and red line indicates median of the distribution. The sample size for each distribution is given in % in (a) and is same for the rest. Missing data are excluded.

coefficient. This is illustrated for the H_s and H_l in Figure 6a. For H_s, the warm (red symbols) versus cold (blue symbols) eddy is apparent in the sea-air temperature difference. The EC and ID flux estimates cluster about the bulk flux line with variability that is typical for 10-min samples. There is some hint of a high bias. The scatter about the bulk flux line is similar in magnitude to the sensible fluxes, but there is no obvious bias. By removing the velocity forcing factor, this presentation makes clear the effects of the thermodynamic forcing and suggest that the bulk flux calculations give reasonable estimates of the fluxes over the eddies. However, there may be issues with different sampling by bulk fluxes (which are computed from T_s right at the ship) versus the turbulent fluxes measured at 20-m height that are characterized by an upwind footprint as much as 0.5 km from the ship. Also, near the edge of a T_s gradient, the turbulent fluxes may be driven by a substantially different T_s and q_s.

The second method is through distributions of 10-min COARE 3.5 bulk fluxes over six atmospheric/oceanic states: voyage including eddies, voyage without eddies, the cold eddy, the warm eddy, no-rain conditions, and rainy conditions are shown in Figure 6b. Further, Table 4 depicts the mean bulk fluxes and flux-related state variables for these six states. It is noted that these forcings are not independent and it is extremely difficult to single out the effect of each forcing with our limited samples. For instance, precipitation events and frontal passages occurred over the mesoscale ocean eddies as well.

The results show that U_{10} is higher by 26.3% over the warm eddy and lower by 3.6% over the cold eddy as compared to average voyage values. The average τ over the warm eddy is higher (mean 0.39 N/m^2) than that over the cold eddy (mean 0.19 N/m^2) and the entire voyage (mean 0.21 N/m^2). Compared with the overall mean for the voyage (1.5×10^{-3}), the mean C_{d10n} is higher over the warm eddy (1.8×10^{-3}) and lower over the cold eddy (1.4×10^{-3}) as reported by White and Annis (2003) as well. The air-sea temperature difference,

Table 4
Mean Bulk Fluxes and Flux-Related State Variables Corresponding to Six Categories as Discussed in Section 3.3

	Voyage	Without eddies	Cold eddy	Warm eddy	No rain	Rain
U_{10n}	10.2396	9.3348	10.6126	13.3147	9.4825	11.7376
τ	0.2104	0.1665	0.1986	0.3982	0.1650	0.3001
T_a	9.4807	10.2721	8.9224	7.0986	9.6274	9.1902
T_s	10.4988	11.5789	8.2041	9.2209	10.8987	9.7076
ΔT	1.0174	−1.3068	0.7182	−2.1248	−1.2700	−0.5174
H_s	12.1593	15.3084	−14.9620	34.8673	13.7658	8.9803
q_a	6.0557	6.2840	6.3024	4.8431	5.7639	6.6337
q_s	7.8449	8.3624	6.7208	7.2645	8.0326	7.4736
Δq	1.7886	2.0785	0.4183	2.4216	2.2680	0.8399
H_l	59.4618	65.1879	5.8216	106.3480	70.4262	37.7650

Note. Refer to Appendix for full variable names and units.

ΔT ranges from −3.2 °C to 3.9 °C over the cold eddy and from −7.7 °C to 1.8 °C over the warm eddy. Mean γ_w is higher by 33% over the warm eddy and by 19% during rainy conditions as compared to the average voyage values. Further, the mean net enthalpy flux ($H_s + H_l$) over the warm eddy (~141.2 W/m^2) is nearly 15 times greater in magnitude than over the cold eddy (~−9.14 W/m^2). The mean net hourly air-sea flux for the voyage without eddies is 80.4 W/m^2, higher than for the voyage with eddies (71.6 W/m^2). Despite the increase in wind stress, both H_s and H_l (mean 8.9 and 37.7 W/m^2, respectively) decrease during rain events as compared to no-rain conditions (mean H_s as 13.7 W/m^2 and H_l as 70.4 W/m^2) during the voyage. Conclusively, γ_w, τ, H_s, and H_l increase by approximately 33%, 89%, 187%, and 79%, respectively, over the warm eddy and decrease by approximately 3%, 5%, 223%, and 90%, respectively, over the cold eddy as compared to the mean voyage values.

3.4. Rain Heat Flux (H_r) Variations

Low-intensity rainfall events (<5 mm/hr) accounted for 80.7% of total frequency of rainfall events, compared with 1.5% of heavy (5–10 mm/hr) and 0.7% of very heavy (>10 mm/hr) rainfall events. On average, H_r remains largely positive and equal to H_s and much smaller than H_l (Figure 7). The positive H_r indicates that the raindrops are colder than T_s, transporting heat from ocean to atmosphere, that is, cooling the ocean surface (Gosnell et al., 1995). Over the cold eddy, it has been found to be mostly negative along with both H_s and H_l.

It is observed that although H_r remains small (~2 W/m^2) for low intensity rainfall (<5 mm/hr), it increases with increasing rain rate and becomes large, nearly of the order of the H_l or larger (>100 W/m^2) during the infrequent heavy rainfall events (>20 mm/hr) over the SO as shown in Figure 7. H_r varied considerably over the cold and warm eddies. Over the cold eddy, H_r remains small <10 W/m^2 with average −1.5 W/m^2 irrespective of the rain rate. However, over the warm eddy, H_r is much higher (mean 111 W/m$^{2)}$ for rain rates greater than 10 mm/hr. For rain rates greater than 20 mm/hr, H_r becomes even larger than H_l with a difference of more than 20 W/m^2. A closer analysis reveals that T_a remains lower than T_s over the warm eddy during both rain and no-rain conditions. The negative H_l occurs when $T_a > T_s$ and $q_a > q_s$ leading to fog conditions and negative H_r (i.e., lower T_s than temperature of raindrops transporting heat into the ocean). Negative values of H_l were observed 43% of the time when the ship was over the cold eddy compared with only 6% of the time for the entire voyage. These results indicate that the cold eddy (warm eddy, respectively) is contributing to net heat gain (net heat loss, respectively) to the ocean even during precipitation events, the magnitude of which increases with increasing rain rate.

3.5. Marine Atmospheric Boundary Layer Stability and Flux Variability

Static stability affects the convection in the boundary layer and can be used in conjunction with the momentum and heat flux variability to characterize the marine atmospheric boundary layer stability (Archer et al., 2016). As per Monin-Obukhov Similarity Theory, the Monin-Obukhov dimensionless stability parameter, ξ, is defined as z/L where z is the height of measurement and L is the Obukhov length, and plays a significant

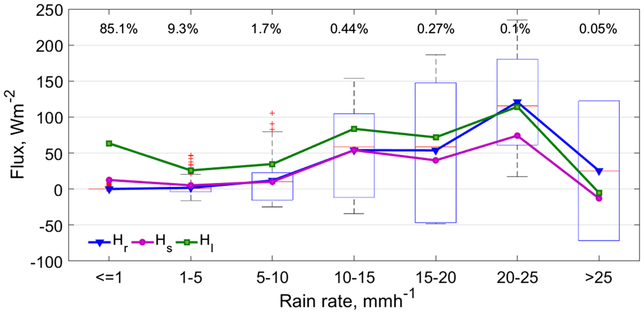

Figure 7. Distribution rain heat flux (H_r) along with mean values for each bin during the voyage classified on rain rate, R (mm/hr), using 10-min flux values. Mean values of H_s and H_l are also plotted for each bin. The percent of data is mentioned for each distribution out of all rain events, that is, when $R > 0$ mm/hr.

role in the computation of surface fluxes (Bradley & Fairall, 2006). Here, we report the variability of fluxes in different stability regimes. It determines the stratification in the surface layer (Foken, 2008) with the following classification (Figure 8) used in this paper: (i) $\xi < -1$ very unstable, (ii) $-1 < \xi < -0.005$ unstable, (iii) $-0.005 < \xi < 0$ unstable close to neutral, (iv) $0 < \xi < 0.005$ stable close to neutral, (v) $0.005 < \xi < 1$ stable, and (vi) $\xi > 1$ very stable. The values of stability parameter during the voyage are mostly concentrated between −1 and −0.005, corresponding to an unstable atmosphere, promoting forced convection. This is not unusual over the ocean surface where the sea surface is generally warmer than the air. Mostly stable stratification is dominant over the cold eddy as the air is often warmer than the ocean (mean ~0.7 °C), in contrast to over the warm eddy where ΔT is found to be lowest (i.e., where the air-sea temperature difference was −2.12 °C) causing unstable stratification. It is also noticeable that unstable conditions prevail irrespective of rainy or nonrainy conditions. The stable stratification is also observed in the warm sector of extratropical cyclones. The stability parameter, ξ, is observed to be mostly negative (average −0.14) implying unstable stratification during preconditions but in the warm sector or midst conditions stable stratification (average 0.24) is observed which again reverts to unstable (average −0.36) in the postfrontal conditions.

Sixty-three percent of the total τ samples are concentrated at $-1 < \xi < -0.005$ with a mean of 0.22 N/m^2. However, mean τ peaks (0.4 N/m^2) during stable close to neutral conditions, that is, when $0 < \xi < 0.005$. These peaks correspond to warm sector of the extratropical cyclones during cold eddy sampling. Further, both H_s and H_l peak with means of 26.8 and 90.2 W/m^2, respectively, during unstable stratification when $-1 < \xi < -0.005$. We note that the sample size is small (<1%) during stable stratification when $\xi > 1$. During stable stratification, that is, $\xi > 0.005$, H_s is strictly negative (mean −18.7 W/m^2) and H_l is mostly negative with a mean of −9.3 W/m^2, that is, directed toward the ocean.

3.6. Extratropical Cyclonic Storms and Flux Variability

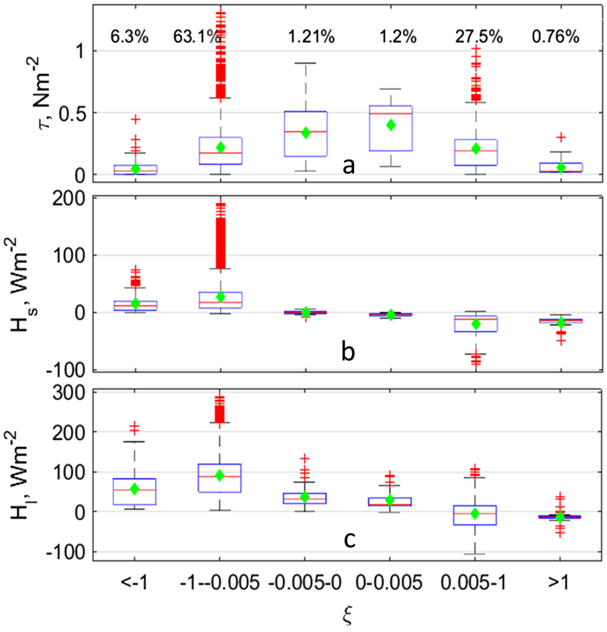

Figure 8. Distributions of (a) wind stress, τ; (b) sensible heat flux, H_s; and (c) latent heat flux, H_l, categorized on the Monin-Obukhov stability parameter ($\xi = z/L$). The percent of data for each distribution is given for τ (same for H_s and H_l). Missing data are excluded.

The location and timing of surface heat and moisture fluxes affect the cyclone evolution and development (Persson et al., 2005, 2008). Figure 9 displays H_s, H_l, and τ distributions during precondition, postcondition, and midst condition over the passage of six extratropical cyclones during the voyage. As concluded from the six cases, mean ΔT changes from −0.88 °C during preconditions to 0.75 °C during midst conditions followed by a sharp decrease of −2.08 °C after the cold front arrives (figures not included). Mean γ_w is observed to negligibly decrease (by <1%) from precondition to midst conditions but increases behind the front by 13.8%. Approximately 1-hr lagged ocean response to the storms is observed; however, the pattern of lagged γ_w does not differ signifcantly.

U_{10} and τ increase during midst conditions as compared to preconditions and then decrease in postconditions in most of the cases. Mean τ increases from 0.18 N/m^2 in preconditions to 0.3 N/m^2 in the midst and then falls to 0.27 N/m^2. Despite the increase in U_{10}, both H_s and H_l values decline significantly during midst conditions. The reduction in H_s is due to a rise in T_a, which affects and sometime changes the sign of ΔT. Likewise, the reduction of H_l is due to moistening in the warm sector. The mean air-sea specific humidity difference, Δq, increases from −1.8 to −0.32 (i.e., the air is moistening toward saturation with respect to the surface value) in warm sector then decreases to −2.8 during postconditions. At times, the moistening causes the surface layer to saturate leading to fog formation. The heat fluxes rise subsequently following the passage of the cold front and a dip in T_a (mean 7.8 °C in postcondition). The mean H_s and H_l reach

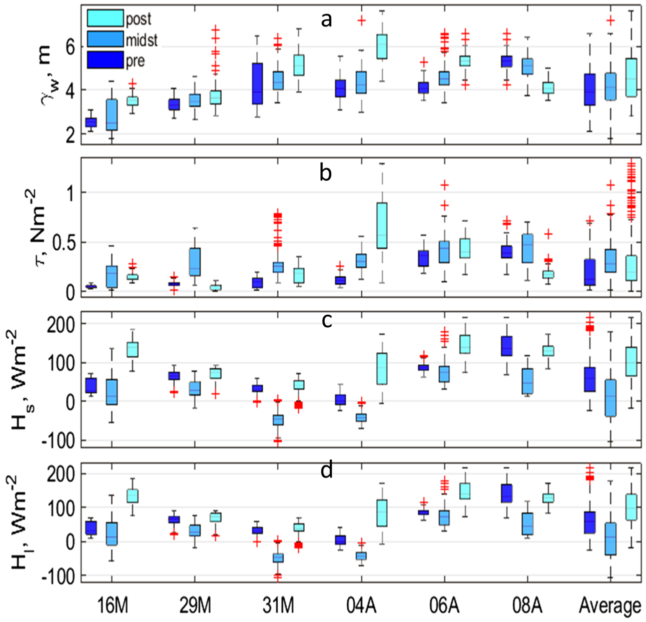

Figure 9. (a) Wind-sea significant wave height, γ_W; (b) wind stress, τ; (c) sensible heat flux, H_S; and (d) latent heat flux, H_l, distributions using COARE 3.5 data shown here as box plots as noted during precondition, midst, and postcondition of six extratropical cyclones. The x axis represents the dates where Suffix-M is for March and Suffix-A is for April month, respectively. The average distributions of fluxes are calculated by combining all predistribution, midst, and postdistribution separately.

a minimum in the midst conditions with means of −13.4 and 13.1 W/m^2, respectively. The fluxes rise dramatically (mean 27.2 and 98.2 W/m^2, respectively) behind the cold front. The minimum H_s and H_l values in the midst are observed over the cold eddy (31 March and 04 April). Conclusively, an increase in τ (~62% average) and a decline in H_s (~235%) and H_l (~79%) is noted in the warm sector, compared to prestorm conditions. This pattern reverses behind the cold front as τ decreases by ~11% but H_s and H_l increase by ~303% and ~647%, respectively, compared to the warm sector values as observed in the present study. In the warm sector, τ ranged from 0.01 to 1.07 N/m^2 which is less intense than that observed over the Atlantic Ocean (Persson et al., 2008). However, heat fluxes show large variations in the warm sector with H_s of −91–103 W/m^2 and H_l of −105–180 W/m^2.

4. Discussion

1. COARE 3.5 model performance is assessed by comparing direct and model derived neutral transfer coefficients as a function of 10-m neutral wind speed. Due to limited sample size, we cannot address the variability of coefficients at either low (<3 m/s) or high (>20 m/s) wind speeds. C_{e10n} measurements show limited variability with winds speed, which is consistent with DeCosmo et al. (1996), Persson et al. (2005), and COARE model. Although C_{h10n} does show an increase with wind speed above 7 m/s as with Persson et al. (2005), the increase is significantly larger and the results are suspect due to issues with sonic temperature as discussed in Appendix B. In COARE 3.5, both C_{e10n} and C_{h10n} are assumed to be the same. However, these results indicate that C_{e10n} and C_{h10n} behave differently and should be studied further.
2. The sea-state dependency of the momentum flux is analyzed through the sea surface roughness length and wave-age parameterization as given in equation ((2)). A slightly higher value of the numerical constant, D, is noted as compared to 0.09 in COARE 3.5, which might affect the evaluation of the Charnock coefficient. Edson et al. (2013) found $D = 0.09$ to be a good fit for all sea states. However, this value might be higher for a sea state dominated by younger waves and vice versa. During CAPRICORN 2016, a fully developed sea with an inverse wave age of less than 0.03 was common over the SO (61% of all times). A mixed sea state composed of both wind sea waves and swell is frequent between 43° and 53°S of the SO (Hanley et al., 2011). Consequently, one single D value might not be representative of total wave influence on surface stress or universally applicable.
3. Despite nominal changes in U_{10} and τ over the cold eddy, as compared to the mean voyage values, a significant decrease is noted in mean heat flux values. Over the warm eddy, on the other hand, a significant increase is observed in mean τ, H_s, and H_l. Modifications in near-surface winds and wind stress due to mesoscale sea surface temperature anomalies have been well documented (Chelton, 2004; Frenger et al., 2013; Park et al., 2006; White & Annis, 2003). However, the magnitudes of changes in surface winds, wind stress, and heat fluxes over the warm and cold eddy measurably differ. Surface heat fluxes over isolated eddies in the SO region are also observed to be far stronger than the climatological flux means in the energetic regions in the South Atlantic Ocean (Bôas et al., 2015). These observations of large fluxes over the SO mesoscale eddies might be governed by the sea surface temperature anomaly arising from the ocean polar front in the SO as well as lifetime and evolution stage of the ocean eddy. During the sampling, the cold eddy had reached past its mature stage and had entered its decay phase impacting its amplitude (Patel et al., 2019). The warm eddy, however, was a short-lived eddy and shifted its center quickly as per the altimetry observations. Thus, precise quantification of the air-sea fluxes over the life cycle of mesoscale eddies in the SO at high spatiotemporal resolution might fill the potential gaps in the uncertainties in the atmospheric heat budget.
4. Although duration limited, H_r increases with rain rate and becomes of the order of H_s and higher for rain rate >5 mm/hr. H_r also becomes as large as H_l and higher for rain rate >20 mm/hr. Higher mean rain rate

and mean H_r are observed over the warm eddy. However, high rain rates are rare and light precipitation (<1.5 mm/hr) dominates the SO as observed by Wang et al. (2015). The region is also renowned for secondary ice production as observed in previous studies (Huang et al., 2017; Mace & Protat, 2018), which might produce much higher H_r if hail were to reach the ocean. This aspect remains unaccounted for in the COARE 3.5 model.

5. Stable stratification is not a common occurrence over the SO sector and was primarily observed over the cold eddy and in the warm sector of frontal passages. τ and U_{10} are highest during stable close to neutral regime ($0 < \xi < 0.005$), whereas H_s and H_l peak in the weakly unstable regime ($-1 < \xi < -0.005$). Enhancement in turbulence due to detached atmospheric eddies has been observed (Sahlee et al., 2008; Smedman et al., 2007) under convective conditions when $L < -150$ m over both land and sea. An alternate flux model over sea was also suggested by Rutgersson et al. (2007) considering this regime. However, our results suggest that sensible and latent heat fluxes peak when $L < -20$ m (when z = 21 m) or $L < -10$ m (when z = 10 m) in the SO. Thermal or moisture roughness length did not corroborate to this peak in the heat fluxes.
6. The ocean-atmosphere state and the extratropical storms in the SO are distinct from those of the North Atlantic and North Pacific (e.g., Hoskins & Hodges, 2005; Huang et al., 2015). In general, the wintertime cold air outbreak events experienced in the northern hemisphere are larger and stronger (Fletcher et al., 2016). The momentum and heat flux variations in the warm sector and postfrontal regimes of the extratropical cyclones during the voyage are in accordance with the results from Persson et al. (2005) over the Atlantic Ocean. However, the rise in q_a did cause negative H_l in all six cases contrary to Persson et al. (2005). The heat flux variations are also more intense than those observed by Persson et al. (2008) in the warm sector. Although heat fluxes always decrease in the warm sector, they remain almost always negative over the cold eddy despite similar changes in T_a and q_a in all six cyclones. These results suggest that the extratropical cyclones in conjunction with the mesoscale ocean eddies have a significant compound effect on the surface heat fluxes. Previous studies have suggested a probable coupling between mesoscale SST anomalies and synoptic storms (Small et al., 2008; Su et al., 2018) affecting air-sea fluxes. While surface heat fluxes are crucial in cyclogenesis (Yokoyama & Yamamoto, 2019), the cyclonic development stage might modulate flux variability too. However, more observations are needed to segregate individual processes.

5. Conclusion

The CAPRICORN 2016 experiment provided unprecedented observations of air-sea interaction over the lower latitudes of the Southern Ocean from Hobart (43°S) to the edge of the Subantarctic Front near 53°S. Although the voyage lasted only for a month (14 March to 15 April 2016), it was the first time such high-quality air-sea flux observations were collected using NOAA PSD flux system over this sector of the Southern Ocean. The experiment facilitated the performance assessment of COARE 3.5 bulk parameterization model over the Southern Ocean region. Prior to this, the NOAA flux system was deployed during the Southern Ocean Gas Exchange Experiment (GasEx) which was carried out in the southwest Atlantic sector of the Southern Ocean (50°S, 40°W) in 2008 (Edson et al., 2011).

Despite the limited observations, our analysis reveals that the ocean and atmosphere processes often cannot be isolated from one another. Nevertheless, our study offers fresh insights into the air-sea interaction processes in the Southern Ocean and provides some fundamental basics for evaluating atmosphere and ocean models over a poorly observed but climatically important region.

Appendix A: List of Variables

γ	significant wave height of full sea, m
γ_w	significant wave height of wind sea waves, m
γ_s	significant wave height of swell waves, m
u_*	friction velocity, m/s
C_p	phase speed of dominant waves, m/s
T_p	spectral peak period, s
g	gravitational acceleration, m/s^2

U_{10}	10-m wind speed, m/s
U_{10n}	10-m neutral wind speed, m/s
F_w	separation or cutoff frequency
t	time, s
P	pressure, hPa
T_a	air temperature, °C
T_s	sea surface temperature, °C
W	wind direction, radian
ρ	air density, kg/m^3
L_v	latent heat of vaporization, J/kg
C_d	drag coefficient
C_h	sensible heat transfer coefficient or Stanton number
C_e	latent heat transfer coefficient or Dalton number
c_p	isobaric specific heat of air, J kg^{-1} K^{-1}
θ	potential temperature, K
q_a	air specific humidity, g/kg
q_s	sea surface saturation specific humidity, g/kg
Δq	sea surface saturation and air specific humidity difference, g/kg
H_s	sensible heat flux, W/m^2
H_l	latent heat flux, W/m^2
H_r	rain heat flux, W/m^2
τ	wind stress or momentum, N/m^2
w	vertical wind velocity, m/s
U_g	gustiness, m/s
G	gustiness factor, m/s
R	rain rate, mm/hr
c_{pw}	specific heat capacity of liquid water, J kg^{-1} K^{-1}
α_w	Clausius-Clayperon wet-bulb factor
ΔT	air and sea surface temperature difference, °C
B_o	bulk Bowen ratio
z_0^{rough}	roughness length for rough flow, m
z_0^{smooth}	roughness length for smooth flow, m
z_0	total roughness length, m
κ	von Kármán's constant, dimensionless
ν	kinematic viscosity of air, m^2/s
z	height, m
L	Obukhov length, m
ξ	Monin-Obukhov stability parameter, dimensionless

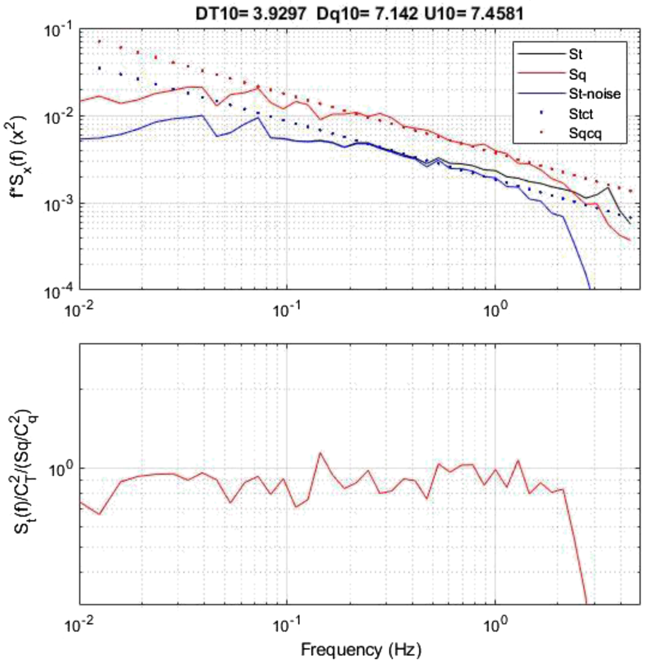

Figure B1. (top) Average variance spectra for temperature (blue) and humidity (red) for 14 10-min samples with sea-air temperature difference (ΔT_{10}) between 3 and 5 °C. The dotted lines are (B2) using the mean of our estimated structure function values for the sample. (bottom) The ratio of the S_t/C_t^2 to S_q/C_q^2; this ratio should be close to 1.0.

Appendix B: Temperature and Humidity Variance Spectra and Inertial Dissipation (ID) method

Inertial-dissipation (ID) flux estimates are based on the Monin-Obukhov Similarity scaling relationship between the turbulent structure function parameter, C_x^2, for the variable, X (u, v, w, T, q) and MOS scaling parameter, x_*,

$$C_x^2 = z^{-2/3} x_*^2 f_x(z/L) \tag{B1}$$

where $x_* = -\overline{w'x'} / \sqrt{-\overline{w'u'}}$ and $f_x(z/L)$ describes the stability dependence (L is the MO length). The structure function values are obtained from fit to the frequency spectrum of X. In the inertial subrange, the spectrum is expected to obey

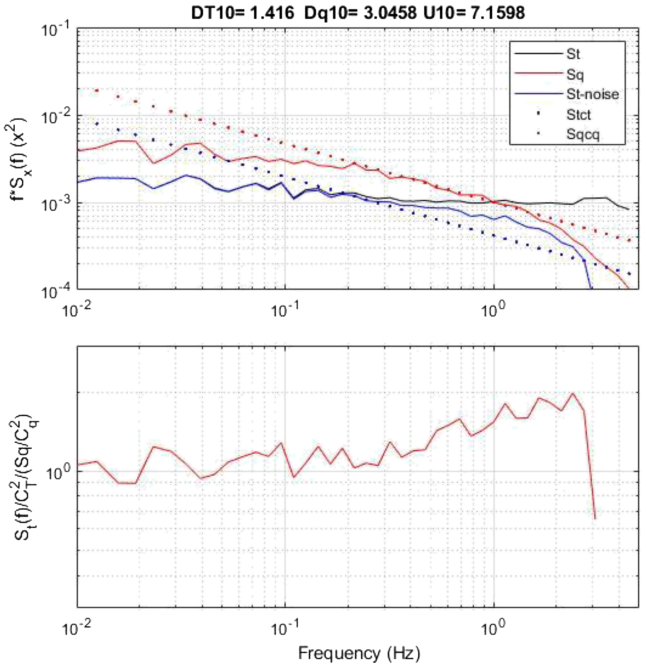

Figure B2. (top) Average variance spectra for temperature (blue) and humidity (red) for 60 10-min samples with sea-air temperature difference (ΔT_{10}) between 1 and 2 °C. The dotted lines are (B2) using the mean of our estimated structure function values for the sample. (bottom) The ratio of the $S_t/{C_t}^2$ to $S_q/{C_q}^2$; this ratio should be close to 1.0.

$$S_x(f) = 0.25C_x^2\left(\frac{U_r}{2\pi}\right)^{2/3}f^{-5/3} \tag{B2}$$

where 0.25 is a mathematical constant and U_r is the relative wind speed. The inertial subrange occurs frequencies where the turbulent fluctuations are approximately isotropic, usually frequencies greater than $f_i = 0.5\ z/U_r$ (Kaimal et al., 1972), where z is the height of the sensor. Above f_i the spectrum follows the −5/3 power law until the dissipation scale is reached (usually $f > 100$ Hz).

We can use observed atmospheric spectra with (B2) to estimate C_x^2 and (B1) is used to compute x_* and the flux is given by

$$\overline{w'x'} = -x_*u_* \tag{B3}$$

The determination of C_x^2 is affected by experimental issues associated with the turbulent sensors: noise, spectral distortion, path averaging, and internal processing/filtering. Path averaging and low-pass filtering typically cause the spectrum to be distorted at frequencies below the Nyquist frequency. So the spectrum will often decrease faster than $f^{5/3}$ approaching the Nyquist frequency. In condition of weak forcing, the spectrum may decline until the broadband noise level of the sensor is reach and then it will flatten. With sonic anemometers, this rarely happens for S_u, S_v, and S_w but occurs occasionally for S_q and is common for S_t. In order to improve the rendition of the inertial subrange, we subtract a white noise level from S_t. However, if the noise level is significant at f_i, then estimates of the temperature structure function become uncertain.

It turns out that the Metek sonic anemometer we used on CAPRICORN 2016 has some undesirable behavior in low signal conditions. To illustrate this, we show mean temperature spectra from the sonic anemometer and mean humidity spectra from the LICOR hygrometer. Figure B1 shows mean temperature and humidity spectra for conditions with strong forcing of temperature fluctuations (large sea-air temperature difference). Both T and q show substantial regions with the expected inertial-subrange slope; f_i is on the order of 0.2 Hz ($f_i\ z/U_r = 0.53$). The humidity spectrum shows path averaging beginning about 1.5 Hz. The raw temperature spectrum does not show much of a −5/3 region, but with the noise removed (S_t-noise), the shape is similar to humidity. This is indicated by normalizing each spectrum by its mean structure function values and taking the ratio (Figure B1, bottom panel). Because of surface-layer similarity, this ratio is expected to be near 1.0.

Spectra with weaker forcing are shown in Figure B2. The humidity spectrum is still well behaved but even the noise-corrected temperature spectrum fails to show a clear −5/3 region. The ratio given in the bottom panel of Figure B2 indicates problems above 0.2 Hz. Thus, the ID sensible heat flux values become questionable for $\Delta T_{10} < 1.5$ °C. For $\Delta T_{10} < 1$ (not shown), the spectra are unusable.

Acknowledgments

This research is supported by ARC Centre of Excellence for Climate System Science (grant DP150102894). PSD participation was supported by NOAA's Climate Program Office, Climate Observation Division. All the data used are listed in the references. The authors wish to thank the CSIRO Marine National Facility (MNF) for its grant of sea time on "*Investigator*" and associated personnel, scientific equipment, and data management. Finally, we would like to acknowledge the crucial roles played by Tom Trull (CSIRO), the lead chief scientist, Tegan Sime, the MNF voyage manager, and the *Investigator* crew to make this research voyage a success. The first author thanks the Editor, reviewer James Edson, and one anonymous reviewer for their extensive and constructive comments on an earlier version of this manuscript, which had helped us to improve the quality of this research article. CAPRICORN 2016 data archive is available from NOAA (gov.noaa.nodc:0170257).

References

Andreas, E. L., & Monahan, E. C. (2000). The Role of Whitecap Bubbles in Air–Sea Heat and Moisture Exchange. *Journal of Physical Oceanography*, *30*, 433–442. https://doi.org/10.1175/1520-0485(2000)030<0433:TROWBI>2.0.CO;2

Archer, C. L., Colle, B. A., Veron, D. L., Veron, F., & Sienkiewicz, M. J. (2016). On the predominance of unstable atmospheric conditions in the marine boundary layer offshore of the U.S. northeastern coast. *Journal of Geophysical Research: Oceans*, *120*, 3372–3380. https://doi.org/10.1002/2015JC011421.Received

Bariteau, L., Fairall, C., Blomquist, B., & Pezoa, S. (2018). CAPRICORN 2016 Field campaign: surface meteorological data and turbulent fluxes collected from the RV Investigator by the National Oceanographic and Atmospheric Administration (NOAA) in the Indian and South Pacific Oceans from 2016-03-14 to 2016-04-15 (NC, https://doi.org/10.7289/V5Q81BBC).

Beare, R. J. (2007). Boundary layer mechanisms in extratropical cyclones. *Quarterly Journal of the Royal*, *133*(October), 503–515. https://doi.org/10.1002/qj

Bôas, A. B. V., Sato, O. T., Chaigneau, A., & Castelão, G. P. (2015). The signature of mesoscale eddies on the air-sea turbulent heat fluxes in the South Atlantic Ocean. *Geophysical Research Letters*, *42*, 1856–1862. https://doi.org/10.1002/2015GL063105.1

Bourassa, M. A., Gille, S. T., Bitz, C., Carlson, D., Cerovecki, I., Clayson, C. A., et al. (2013). High-latitude ocean and sea ice surface fluxes: Challenges for climate research. *Bulletin of the American Meteorological Society*, *94*(3), 403–423. https://doi.org/10.1175/BAMS-D-11-00244.1

Bradley, F., & Fairall, C. (2006). A guide to making climate quality meteorological and flux measurements at sea. *NOAA Technical Memorandum*, *OAR PSD-31*(October).

Brunke, M. A., Fairall, C. W., Zeng, X., Eymard, L., & Curry, J. A. (2003). Which Bulk Aerodynamic Algorithms are Least Problematic in Computing Ocean Surface Turbulent Fluxes? *Journal of Climate*, *16*(4), 619–635. https://doi.org/10.1175/1520-0442(2003)016<0619:WBAAAL>2.0.CO;2

Cerovečki, I., Talley, L. D., & Mazloff, M. R. (2011). A comparison of southern ocean air-sea buoyancy flux from an ocean state estimate with five other products. *Journal of Climate*, *24*(24), 6283–6306. https://doi.org/10.1175/2011JCLI3858.1

Chelton, D. B. (2004). Satellite Measurements Reveal Persistent Small-Scale Features in Ocean Winds. *Science*, *303*(5660), 978–983. https://doi.org/10.1126/science.1091901

Curry, J. A., Bentamy, A., Bourassa, M. A., Bourras, D., Bradley, E. F., Brunke, M., et al. (2004). Seaflux. *Bulletin of the American Meteorological Society*, *85*(3), 409–424. https://doi.org/10.1175/BAMS-85-3-409

DeCosmo, J., Katsaros, K. B., Smith, S. D., Anderson, R. J., Oost, W. A., Bumke, K., & Chadwick, H. (1996). Air-sea exchange of water vapor and sensible heat: The Humidity Exchange Over the Sea (HEXOS) results. *Journal of Geophysical Research, Oceans*, *101*(C5), 12,001–12,016. https://doi.org/10.1029/95JC03796

Dobson, F. W., Smith, S. D., & Anderson, R. J. (1994). Measuring the relationship between wind stress and sea state in the open ocean in the presence of swell. *Atmosphere-Ocean*, *32*(1), 237–256. https://doi.org/10.1080/07055900.1994.9649497

Donelan, M. A., Dobson, F. W., Smith, S. D., & Anderson, R. J. (1993). On the Dependence of Sea Surface Roughness on Wave Development. *Journal of Physical Oceanography*, *25*(8), 2143–2149. https://doi.org/10.1175/1520-0485(1995)025<1905:CODOSS>2.0.CO;2

Dong, S., Gille, S. T., & Sprintall, J. (2007). An assessment of the Southern Ocean mixed layer heat budget. *Journal of Climate*, *20*(17), 4425–4442. https://doi.org/10.1175/JCLI4259.1

Drennan, W. M., Taylor, P. K., & Yelland, M. J. (2005). Parameterizing the Sea Surface Roughness. *Journal of Physical Oceanography*, *35*(5), 835–848. https://doi.org/10.1175/JPO2704.1

Dupuis, H. (2003). Impact of flow distortion corrections on turbulent fluxes estimated by the inertial dissipation method during the FETCH experiment on R/V *L'Atalante*. *Journal of Geophysical Research*, *108*(C3). https://doi.org/10.1029/2001jc001075

Edson, J. B., Fairall, C. W., Bariteau, L., Zappa, C. J., Cifuentes-Lorenzen, A., McGillis, W. R., et al. (2011). Direct covariance measurement of CO2gas transfer velocity during the 2008 Southern Ocean Gas Exchange Experiment: Wind speed dependency. *Journal of Geophysical Research, Oceans*, *116*(11), 1–24. https://doi.org/10.1029/2011JC007022

Edson, J. B., Jampana, V., Weller, R. A., Bigorre, S. P., Plueddemann, A. J., Fairall, C. W., et al. (2013). On the Exchange of Momentum over the Open Ocean. *Journal of Physical Oceanography*, *43*(8), 1589–1610. https://doi.org/10.1175/JPO-D-12-0173.1

Fairall, C. W., Bradley, E. F., Hare, J. E., Grachev, A. A., & Edson, J. B. (2003). Bulk parameterization of air-sea fluxes: Updates and verification for the COARE algorithm. *Journal of Climate*, *16*(4), 571–591. https://doi.org/10.1175/1520-0442(2003)016<0571:BPOASF>2.0.CO;2

Fairall, C. W., Bradley, E. F., Rogers, D. P., Edson, J. B., & Young, G. S. (1996). Bulk parameterization of air-sea fluxes for Tropical Ocean-Global Atmosphere Coupled-Ocean Atmosphere Response Experiment. *Journal of Geophysical Research*, *101*(C2), 3747. https://doi.org/10.1029/95JC03205

Fairall, C. W., Edson, J. B., Larsen, S. E., & Mestayer, P. G. (1990). Inertial-Dissipation Air-Sea Flux Measurements: A Prototype System Using Realtime Spectral Computations. *Journal of Atmospheric and Oceanic Technology*, *7*(3), 425–453. https://doi.org/10.1175/1520-0426(1990)007<0425:IDASFM>2.0.CO;2

Fairall, C. W., White, A. B., Edson, J. B., & Hare, J. E. (1997). Integrated shipboard measurements of the marine boundary layer. *Journal of Atmospheric and Oceanic Technology*, *14*(3), 338–359. https://doi.org/10.1175/1520-0426(1997)014<0338:ISMOTM>2.0.CO;2

Fletcher, J., Mason, S., & Jakob, C. (2016). The climatology, meteorology, and boundary layer structure of marine cold air outbreaks in both hemispheres. *Journal of Climate*, *29*(6), 1999–2014. https://doi.org/10.1175/JCLI-D-15-0268.1

Foken, T. (2008). In C. J. Nappo (Ed.), *Micrometeorology*. Berlin Heidelberg: Springer-Verlag.

Frenger, I., Gruber, N., Knutti, R., & Münnich, M. (2013). Imprint of Southern Ocean eddies on winds, clouds and rainfall. *Nature Geoscience*, *6*(8), 608–612. https://doi.org/10.1038/ngeo1863

Gilhousen, D. B., & Hervey, R. (2002). Improved Estimates of Swell from Moored Buoys. In B. L. Edge & J. M. Hemsley (Eds.), *Ocean Wave Measurement and Analysis* (pp. 387–393). Reston: American Society of Civil Engineers. https://doi.org/10.1061/40604(273)40

Gosnell, R., Fairall, C. W., & Webster, P. J. (1995). The sensible heat of rainfall in the tropical ocean. *Journal of Geophysical Research, Oceans*, *100*(C9), 18,437–18,442. https://doi.org/10.1029/95JC01833

Greatbatch, R. J., Zhai, X., Eden, C., & Olbers, D. (2007). The possible role in the ocean heat budget of eddy-induced mixing due to air-sea interaction. *Geophysical Research Letters*, *34*, L07604. https://doi.org/10.1029/2007GL029533

Hande, L. B., Siems, S. T., Manton, M. J., & Belusic, D. (2012). Observations of wind shear over the Southern Ocean. *Journal of Geophysical Research-Atmospheres*, *117*(12), 1–19. https://doi.org/10.1029/2012JD017488

Hanley, K. E., Belcher, S. E., & Sullivan, P. P. (2011). A Global Climatology of Wind–Wave Interaction. *Journal of Physical Oceanography*, *41*(9), 1811–1813. https://doi.org/10.1175/jpo-d-10-05015.1

Hausmann, U., & Czaja, A. (2012). The observed signature of mesoscale eddies in sea surface temperature and the associated heat transport. *Deep-Sea Research Part I: Oceanographic Research Papers*, *70*, 60–72. https://doi.org/10.1016/j.dsr.2012.08.005

Hausmann, U., Czaja, A., & Marshall, J. (2016). Estimates of air-sea feedbacks on sea surface temperature anomalies in the Southern Ocean. *Journal of Climate*, *29*(2), 439–454. https://doi.org/10.1175/JCLI-D-15-0015.1

Herman, A. (2015). Trends and variability of the atmosphere–ocean turbulent heat flux in the extratropical Southern Hemisphere. *Scientific Reports*, *5*(14900). https://doi.org/10.1038/srep14900

Hoskins, B. J., & Hodges, K. I. (2005). A new perspective on Southern Hemisphere storm tracks. *Journal of Climate*, *18*(20), 4108–4129. https://doi.org/10.1175/JCLI3570.1

Huang, Y., Chubb, T., Baumgardner, D., deHoog, M., Siems, S. T., & Manton, M. J. (2017). Evidence for secondary ice production in Southern Ocean open cellular convection. *Quarterly Journal of the Royal Meteorological Society*, *143*(704), 1685–1703. https://doi.org/10.1002/qj.3041

Huang, Y., Protat, A., Siems, S. T., & Manton, M. J. (2015). A-Train observations of maritime midlatitude storm-track cloud systems: Comparing the Southern Ocean against the North Atlantic. *Journal of Climate*, *28*(5), 1920–1939. https://doi.org/10.1175/JCLI-D-14-00169.1

Jiang, C., Gille, S. T., Sprintall, J., Yoshimura, K., & Kanamitsu, M. (2012). Spatial variation in turbulent heat fluxes in Drake Passage. *Journal of Climate*, *25*(5), 1470–1488. https://doi.org/10.1175/2011JCLI4071.1

Kaimal, J. C., Wyngaard, J. C., Izumi, Y., & Coté, O. R. (1972). Spectral characteristics of surface-layer turbulence. *Quarterly Journal of the Royal Meteorological Society*, *98*(417), 563–589. https://doi.org/10.1002/qj.49709841707

Kawai, Y., & Wada, A. (2007). Diurnal sea surface temperature variation and its impact on the atmosphere and ocean: A review. *Journal of Oceanography*, *63*(5), 721–744. https://doi.org/10.1007/s10872-007-0063-0

Large, W. G., & Pond, S. (1981). open ocean momentum flux measurements in moderate to strong winds. *Journal of Physical Oceanography*, *11*. https://doi.org/10.1175/1520-0485(1981)011<0324:OOMFMI>2.0.CO;2

Large, W. G., & Pond, S. (1982). Sensible and Latent Heat Flux Measurements over the Ocean. *Journal of Physical Oceanography*, *12*(5), 464–482. https://doi.org/10.1175/1520-0485(1982)012<0464:SALHFM>2.0.CO;2

Liu, J., Xiao, T., & Chen, L. (2011). Intercomparisons of air-sea heat fluxes over the Southern Ocean. *Journal of Climate*, *24*(4), 1198–1211. https://doi.org/10.1175/2010JCLI3699.1

Mace, G. G. J., & Protat, A. (2018). Clouds over the Southern Ocean as observed from the R/V *Investigator* during CAPRICORN. Part I: Cloud occurrence and phase partitioning. *Journal of Applied Meteorology and Climatology*, *57*(8), 1783–1803. https://doi.org/10.1175/JAMC-D-17-0194.1

Messager, C., Speich, S., & Key, E. (2012). Marine atmospheric boundary layer over some Southern Ocean fronts during the IPY BGH 2008 cruise. *Ocean Science*, *8*(6), 1001–1023. https://doi.org/10.5194/os-8-1001-2012

Morrow, R., Church, J., Coleman, R., Chelton, D., & White, N. (1992). Eddy momentum flux and its contribution to the Southern Ocean momentum balance. *Nature*, *360*, 40–46.

Olbers, D., Willebrand, J., & Eden, C. (2012). The Circulation of the Southern Ocean. In *Ocean Dynamics* (pp. 1–704). Berlin Heidelberg: Springer-Verlag.

O'Neill, L. W., Chelton, D. B., & Esbensen, S. K. (2003). Observations of SST-induced perturbations of the wind stress field over the Southern Ocean on seasonal timescales. *Journal of Climate*, *16*(14), 2340–2354. https://doi.org/10.1175/2780.1

Park, K. A., Cornillon, P., & Codiga, D. L. (2006). Modification of surface winds near ocean fronts: Effects of Gulf Stream rings on scatterometer (QuikSCAT, NSCAT) wind observations. *Journal of Geophysical Research, Oceans*, *111*(3), 1–19. https://doi.org/10.1029/2005JC003016

Patel, R. S., Phillips, H. E., Strutton, P. G., Lenton, A., & Llort, J. (2019). Meridional Heat and Salt Transport Across the Subantarctic Front by Cold-Core Eddies. *Journal of Geophysical Research: Oceans*, *124*(2), 981–1004. https://doi.org/10.1029/2018JC014655

Persson, P. O. G., Hare, J. E., Fairall, C. W., & Otto, W. D. (2005). Air–sea interaction processes in warm and cold sectors of extratropical cyclonic storms observed during FASTEX. *Quarterly Journal of the Royal Meteorological Society*, *131*(607), 877–912. https://doi.org/10.1256/qj.03.181

Persson, P. O. G., Hare, J. E., Nance, L. B., Walter, B., Noaa, C., & Psd, E. (2008). Impact of Air-Sea Interactions on Extra-Tropical Cyclones, in *ECMWF Workshop on Ocean-Atmosphere Interactions*, pp. 123–146.

Richter, D. H., & Sullivan, P. P. (2014). The Sea Spray Contribution to Sensible Heat Flux. *Journal of the Atmospheric Sciences*, *71*(2), 640–654. https://doi.org/10.1175/JAS-D-13-0204.1

Rutgersson, A., Carlsson, B., & Smedman, A. S. (2007). Modelling sensible and latent heat fluxes over sea during unstable, very close to neutral conditions. *Boundary-Layer Meteorology*, *123*(3), 395–415. https://doi.org/10.1007/s10546-006-9150-9

Sahlee, E., Smedman, A.-S., Hogstrom, U., & Rutgersson, A. (2008). Reevaluation of the Bulk Exchange Coefficient for Humidity at Sea during Unstable and Neutral Conditions, *J. Physical Oceanography*, *38*(1), 257–272. https://doi.org/10.1175/2007JPO3754.1

Schulz, E. W., Josey, S. A., & Verein, R. (2012). First air-sea flux mooring measurements in the Southern Ocean. *Geophysical Research Letters*, *39*, L16606. https://doi.org/10.1029/2012GL052290

Slonaker, R. L., & van Woert, M. L. (1999). Atmospheric moisture transport across the Southern Ocean via satellite observations. *Journal of Geophysical Research*, *104*(D8), 9229–9249. https://doi.org/10.1029/1999JD900045

Small, R. J., DeSzoeke, S. P., Xie, S. P., O'Neill, L., Seo, H., Song, Q., et al. (2008). Air-sea interaction over ocean fronts and eddies. *Dynamics of Atmospheres and Oceans*, *45*, 274–319. https://doi.org/10.1016/j.dynatmoce.2008.01.001

Smedman, A.-S., Ogstr¨om, U. H., Sahl', E., & Johansson, C. (2007). Critical re-evaluation of the bulk transfer coefficient for sensible heat over the ocean during unstable and neutral conditions. *Quarterly Journal of the Royal*, *133*(October), 937–948. https://doi.org/10.1002/qj

Smith, S. D. (1988). Coefficients for sea surface wind stress, heat flux, and wind profiles as a function of wind speed and temperature. *Journal of Geophysical Research, Oceans*, *93*(C12), 15,467–15,472. https://doi.org/10.1029/JC093iC12p15467

Smith, S. D., Anderson, R. J., Oost, W. A., Kraan, C., Maat, N., de Cosmo, J., et al. (1992). Sea surface wind stress and drag coefficients: The HEXOS results. *Boundary-Layer Meteorology*, *60*(1–2), 109–142. https://doi.org/10.1007/BF00122064

Song, X., & Yu, L. (2012). High-latitude contribution to global variability of air-sea sensible heat flux. *Journal of Climate*, *25*(10), 3515–3531. https://doi.org/10.1175/JCLI-D-11-00028.1

Su, Z., Wang, J., Klein, P., Thompson, A. F., & Menemenlis, D. (2018). Ocean submesoscales as a key component of the global heat budget. *Nature Communications*, *9*(1), 1–8. https://doi.org/10.1038/s41467-018-02983-w

Trenberth, K. E., & Fasullo, J. T. (2010). Simulation of present-day and twenty-first-century energy budgets of the southern oceans. *Journal of Climate*, *23*(2), 440–454. https://doi.org/10.1175/2009JCLI3152.1

Trull, T., Schulz, E., Protat, A., & Strutton, P. (2016). *RV Investigator Voyage Summary Voyage*. Hobart. Retrieved from https://www.cmar.csiro.au/data/trawler/survey_list.cfm?q=&source_id=309&start=41#IN2016_V02

Wang, Z., Siems, S. T., Belusic, D., Manton, M. J., & Huang, Y. (2015). A climatology of the precipitation over the Southern Ocean as observed at Macquarie Island. *Journal of Applied Meteorology and Climatology*, *54*(12), 2321–2337. https://doi.org/10.1175/JAMC-D-14-0211.1

White, W. B., & Annis, J. L. (2003). Coupling of Extratropical Mesoscale Eddies in the Ocean to Westerly Winds in the Atmospheric Boundary Layer. *Journal of Physical Oceanography*, *33*(5), 1095–1107. https://doi.org/10.1175/1520-0485(2003)033<1095:COEMEI>2.0.CO;2

Yelland, M. J., Moat, B. I., Taylor, P. K., Pascal, R. W., Hutchings, J., & Cornell, V. C. (1998). Wind Stress Measurements from the Open Ocean Corrected for Airflow Distortion by the Ship. *Journal of Physical Oceanography*, *28*(7), 1511–1526. https://doi.org/10.1175/1520-0485(1998)028<1511:WSMFTO>2.0.CO;2

Yokoyama, Y., & Yamamoto, M. (2019). Influences of surface heat flux on twin cyclone structure during their explosive development over the East Asian marginal seas on 23 January 2008. *Weather and Climate Extremes*, *23*(January), 100198. https://doi.org/10.1016/j.wace.2019.100198

Yu, L., Zhang, Z., Zhong, S., Zhou, M., Gao, Z., Wu, H., & Sun, B. (2011). An inter-comparison of six latent and sensible heat flux products over the southern ocean. *Polar Research*, *30*(SUPPL.1), 1–27. https://doi.org/10.3402/polar.v30i0.10167

Zeng, X., Zhao, M., & Dickinson, R. E. (1998). Intercomparison of bulk aerodynamic algorithms for the computation of sea surface fluxes using TOGA COARE and TAO data. *Journal of Climate*, *11*(10), 2628–2644. https://doi.org/10.1175/1520-0442(1998)011<2628:IOBAAF>2.0.CO;2